a 60° sweep). Accepting a constant attitude system, while allowing minor off-normal solar panel orientation during thrusting, negligibly degrades mission performance. Conceptual designs have been formulated incorporating 360° rotational capability between the plane of the solar cell panels and the basic spacecraft body, but failure of the rotational system will abort the mission. To maintain center of mass stability, the mercury reservoir should be at the vehicle's center of gravity. This implies that the reservoir is the central part of the rotation device between the solar panels and the basic structure. Even if such a mechanical system could be designed well within the 15 kg margin, the reliability factors of such a system do not merit its consideration for the multimission spacecraft design.

Conclusion

Based on the results of low-thrust trajectory analyses for three unique missions (asteroid belt probe, solar probe, and out-of-ecliptic probe), a single set of propulsion system parameters was found that permitted use of a common solar electric propulsion system for multimission SEP spacecraft design. The components in the selected propulsion system design are representative of the present ion propulsion system technology. A single, uncomplicated spacecraft design concept was formulated that has the capability of carrying a large complement of science equipment (approximately 600 lb) for any of the three missions studied. In summary, although optimum performance for each mission is not achieved by a single spacecraft design, only minor modifications to the spacecraft are necessary to efficiently perform any one of the three missions studied. Thus, such a spacecraft appears extremely attractive for near term solar electric propulsion missions using an Atlas (SLV-3C)/Centaur launch vehicle.

References

[1] Meissinger, H. F., Park, R. A., and Hunter, H. M., "A 3 KW Solar-Electric Spacecraft for Multiple Interplanetary Missions," AIAA Paper 67-711, Colorado Springs, Colo., 1967.

[2] "Solar Powered Electric Propulsion Program," Program Summary Report, SSD 60374R, Dec. 1966, Hughes Aircraft Co.

[3] Molitor J. H. et al., "Design of a Solar-Electric Propulsion System for Interplanetary Spacecraft," *Journal of Spacecraft and Rockets*, Vol. 4, No. 2, Feb. 1967, pp. 176–182.

[4] King, H. T., Poeschel, R. L., and Ward, J. W., "2½ kW Low Specific Impulse, Hollow-Cathode Mercury Thruster," AIAA Paper 69-300, Williamsburg, Va., 1969.

[5] Pawlik, E. V., Macie, T. W., and Ferrera, J. D., "Electric Propulsion System Performance Evaluation," AIAA Paper 69-236, Williamsburg, Va., 1969.

[6] Seliger, R. L., Russell, K. J., and Molitor, J. H., "Electric Propulsion Design Optimization Methodology," AIAA Paper 69-254, Williamsburg, Va., 1969.

[7] MacPherson, D., "Mission Analysis Technology," *7th Electric Propulsion Conference*, Vol. 4, AIAA, New York, 1969.

[8] Smith, A. H., Cohn, E. M., and Maxwell, P. T., "Solar Cell Electrochemical Power Supplies—10 watts to 50 kw," Preprint IX E.2, June 1969, American Astronautical Society and DRS.

NOVEMBER 1969 J. SPACECRAFT VOL. 6, NO. 11

Optimal Estimation of Rotation-Coupled Flexural Oscillations

JAMES L. FARRELL,* JAMES K. NEWTON,† JAMES A. MILLER,‡ AND ELIEZER N. SOLOMON§
Westinghouse Defense and Space Center, Baltimore, Md.

The Radio Astronomy Explorer satellite, presently orbiting the Earth and holding an accurate local orientation by four 750-ft booms, experiences significant static and dynamic elastic deformations in orbit. The gravity-gradient librations, which actually are coupled to the flexure at these boom lengths, are observable at close intervals while the boom tips are monitored only when the satellite is within range of certain TV stations. An iterative weighted least-squares estimation program has been developed, in which a time history for the state (attitude, damper displacement, and elastic deformation) is reconstructed, using all pertinent data available. A companion program, capable of generating hypothetical data corrupted by additive Gaussian noise, has been used to demonstrate successful reconstruction, augmented by instrument bias detection and improved determination of certain system parameters. Linearized ensemble statistics have been generated, to predict performance under various conditions.

Nomenclature¶

a_i = solar heat absorptivity of ith antenna ($1 \leqslant i \leqslant 4$)
$\mathbf{A}_i$ = unit vector along sensitive axis of ith magnetometer ($1 \leqslant i \leqslant 3$)
$\mathbf{b}$ = 3×1 vector of magnetometer bias errors
$[B_i]$ = canonical dynamic coefficient matrix during ith interval
$[C']$ = orthogonal transformation from hub principal axes to local coordinates
d = boom diameter
$[d],[m]$ = coefficient matrices for first and second time derivatives, respectively, of generalized coordinates in equations of motion
e = linear thermal expansion coefficient for booms
$\boldsymbol{\mathcal{E}}$ = 5×1 vector of satellite parameters, a_1–a_4; EI
E = boom modulus of elasticity
EI = boom flexural rigidity
$[\mathcal{G}]$ = 24×5 matrix, $\partial\dot{\mathbf{X}}/\partial\boldsymbol{\mathcal{E}}$
$[G_{m,i-1}]$ = integrated effect of variations in $\boldsymbol{\mathcal{E}}$, from beginning of ith interval to time (t_m)
$[H_m],[\mathfrak{M}_m]$ = matrix of partial derivatives of observables with respect to current state and with respect to initial state, respectively

Received November 18, 1968; revision received August 18, 1969. Contract NAS5-9753-20, Goddard Space Flight Center.

* Fellow Engineer, Control Data Systems Section. Associate Fellow AIAA.

† Engineer, Control Data Systems Section. Member AIAA.

‡ Supervisory Engineer, Digital Analysis and Control Section.

§ Associate Engineer, Digital Analysis and Control Section.

¶ Mks units; all angles in radians.

$[I]$ = identity matrix
J_s = solar heat flux
$[k],[\Delta k_t]$ = coefficient matrix for generalized coordinates in equations of motion and augmenting matrix arising from thermal effects, respectively
$\mathfrak{K}_i$ = thermally induced curvature of ith antenna ($1 \leqslant i \leqslant 4$)
l = antenna length
$\mathbf{L}$ = unit normal to sun sensor face plane
m_θ = number of data vectors per fixed-parameter time zone
N_f = degrees of freedom for chi-squared distribution
$N_{p(i)}$ = number of measurements accepted from ith instrumenting channel ($1 \leqslant i \leqslant 14$)
N_θ = minimum number of fixed-parameter time zones per orbit
N_τ = total number of linearized state transition periods in the data block
$\mathbf{p}_i,\mathbf{p}_i',\mathbf{p}_i''$ = vector from hub center to point on ith antenna, unit tangent vector, and curvature, respectively
$[Q_m]$ = covariance matrix for mth data vector error
R = rss of normalized residuals
$R_{L(i)}$ = acceptance limit for residual in ith instrumenting channel ($1 \leqslant i \leqslant 14$)
t_m = time of mth data vector
T_m = hysteresis damper torque
$T_{\mathrm{I}},T_{\mathrm{II}}$ = first- and second-order kinetic energies, respectively
$\mathbf{U}_i$ = unit vector along ith sun sensor slit
$V_{\mathrm{I}},V_{\mathrm{II}}$ = first- and second-order potential energies, respectively
W_j = component of boom tip deflection beyond equilibrium ($1 \leqslant j \leqslant 8$)
$\mathbf{X}$ = state vector
Y,y = observable and residual, respectively
$\mathcal{Z}$ = boom wall thickness
β_i = scaled absorptivity of ith antenna ($1 \leq i \leq 4$)
$\boldsymbol{\beta}_L$ = magnetic field vector in local coordinates
κ = thermal conductivity of antenna booms
σ,σ_L = unit sunline vector in hub and local coordinates, respectively
$\sigma_0,\sigma_{I,j}$ = zero-order component of $\boldsymbol{\sigma}$, and partial derivative of first-order component with respect to X_j, respectively
$\sigma_D,\sigma_F,$ σ_S,σ_W = rms errors in measurements of damper angle, magnetometer, sun sensor, and antenna tips, respectively
σ_i = rms error in ith instrumenting channel ($1 \leqslant i \leqslant 14$)
σ_u = estimation uncertainty parameter in data rejection criteria
τ = fixed-parameter time zone boundary
$[\Phi]$ = state transition matrix
$\boldsymbol{\varphi}$ = state transition vector
$\dot{\boldsymbol{\chi}}$ = vector of generalized coordinates
$\boldsymbol{\Psi}_0$ = total zero-order generalized Lagrange force vector
$\boldsymbol{\Psi}_d,\boldsymbol{\Psi}_e,$ $\boldsymbol{\Psi}_{s0},\boldsymbol{\Psi}_{t0}$ = contribution to $\boldsymbol{\Psi}_0$ by damper, eccentricity, solar pressure, and thermal effects, respectively
$[\ ],[\ ]^{-1}$ = matrix and inverse, respectively
$(\ )^T$ = transpose of $(\ )$
$(\hat{\ })$ = estimated or observed value of $(\ )$
$(\tilde{\ })$ = error in $(\ )$
$(\ )^{(-)}$ = predicted value of $(\ )$
$(\ )^*$ = augmented $(\ )$
$\langle\ \rangle$ = probabilitistic mean

Introduction

THE NASA Goddard Space Flight Center Radio Astronomy Explorer (RAE) satellite[1] is presently in a circular orbit of 5800-km altitude. Its 750-ft-long booms provide three-dimensional gravity-gradient stabilization to within a few degrees of local orientation. Its cruciform configuration also provides for double-V antenna reception of rf data. For proper interpretation of received rf data it is necessary to know the antenna directivity patterns; consequently, large elastic deformations of the booms are of considerable interest to the experimenter. At the same time, only intermittent boom tip observations will be available (i.e., during passes over regions covered by specified TV stations). Filling in the time history during each data gap suggests the use of minimum variance data processing, which in turn calls for a dynamical model in a form amenable to statistical analysis.

Physically the RAE flexural oscillations are coupled to the attitude librations and to the damper displacement; therefore, they are excited by any initial conditions (e.g., oscillations at termination of deployment) or forcing functions (e.g., orbital eccentricity) which affect these angles. Furthermore, certain modes of satellite deformation are driven directly by eccentricity, solar radiation pressure, and/or uneven heating. These latter two items affect the dynamics in a complex manner, since the incident areas for solar pressure and the diametric temperature differentials vary with both 1) position along boom length, and 2) the state itself, i.e., satellite attitude and elastic deformation. Reference 2 describes the coupled dynamics under force-free conditions and Ref. 3 extends this analysis to the nonhomogeneous case; these results were verified[4] through a recently documented digital program[5] that applies the Hooker-Margulies[6] and Roberson-Wittenburg[7] formalism to a discretized model of the structure.

In the present paper the viscous damping of Refs. 2 and 3 is replaced by a saturating magnetic hysteresis device. The resulting short-term dynamic equations still have the form of 12 coupled linear harmonic oscillators with constant parameters and steady driving forces. Behavior over extended periods is obtained by cascading these short-term solutions, allowing discrete coefficient adjustments at the time zone boundaries. As in Ref. 3, the dynamic reference state is near equilibrium, but repeatedly adjusted to points closer to the instantaneous state. This accounts for certain higher-order coupling arising from low-frequency angular displacements, while still allowing the Taylor series to be truncated after first order.

Linearization of the dynamic equations permits implementation of existing data processing techniques in their classical form. Procedures can therefore be drawn from a wealth of related experience (e.g., in orbit determination), but certain guidelines will be decidedly slanted toward this specific application. Satellite attitude and damper displacement are restrained by gravity gradient and a hinge spring, respectively; also, the antenna booms have a specific configuration of static bending deflections for any given set of conditions (solar aspect, etc.). Then, unlike the orbit tracking problem, the rotational and flexural behavior are characterized by a minimum potential energy equilibrium, representing a preferred state at the center of oscillatory motion. This is quite fortunate, since it will have a stabilizing effect upon processed data taken from any stable satellite.

From the preceding considerations there emerges a plan whereby 1) all measurements pertaining to the dynamics of interest (i.e., the boom tip observations plus sun sensor, magnetometer, and damper displacement readings, which are related to these deformations through the dynamic coupling) are arranged in data blocks, and 2) on the basis of all data in any block, a minimum variance estimate can be obtained for the corresponding time history. Procedural details are dictated by the following ground rules.

1) It is permissible for data blocks to overlap, but each block is handled separately in standardized fashion.

2) Choice of block duration is influenced by observability and by modeling accuracy. For example, a few percent deviation from estimated rigidity coefficients of the perforated booms will produce a corresponding difference in flexural frequencies (nominally about three times orbital rate), thereby causing significant drift of phase angles associated with these frequencies. It is therefore desirable to limit data block duration to roughly one orbit, and, to prevent concentration of accumulated extrapolation error, data blocks should be bounded by boom tip observations (with no real time requirement) at both ends.

3) In addition to parameter uncertainties, the model is limited by absence of loosely coupled effects (e.g., higher modes) and anomalies such as inhomogeneities or force-free warpage in antenna booms. Combined with observability limitations in the presence of small high-frequency flexural oscillations, this points to antenna tip estimation accuracies no better than the TV resolution (about one meter). Successful interpolation, rather than redundant measurement error reduction, is the primary objective.

4) Full advantage is taken of all concurrent information. Availability of smoothed navigation data at close intervals enables the effects of orbital perturbations to be taken into account while using a simplified (patched conic) orbit model in the rotational-flexural dynamics. Availability of closely spaced damper angle indicator readings allows the short-term dynamical time zone boundaries to be controlled by switching events in a discrete-torque model which closely approximates the saturating magnetic hysteresis device. This choice of time zones enhances computational efficiency. Computational efficiency is further increased by prefiltering of closely spaced sun sensor and magnetometer observations.

5) Prior to acceptance all measurements are automatically subjected to controllable data conditioning criteria (based upon linearity considerations in connection with partial derivatives[8]) and criteria involving the size of the residual. The normalized residuals will also influence the number of data recycling iterations.

6) If there are long periods without significant reception of radio astronomy data, estimation of rotational-flexural time history during these periods is not necessary. Due to the existence of a reference equilibrium state, iterative data processing can be resumed with zero initial estimates for unknown state vector components.

This paper reports the results of a simulation whereby a minimum variance estimation program is fed by hypothetical data, and converges upon the history of its dynamic behavior while simultaneously detecting certain instrument biases and variations in certain system parameters. This is successfully accomplished with light coverage of the four antennas (i.e., single station coverage of each tip at the beginning and end of an orbit), accompanied by essentially continuous damper, sun sensor, and magnetometer data. As might be expected from the inherent flexibility of minimum variance data processing, various additional capabilities of the basic approach are being discovered. These include extension to nonsimultaneous antenna tip observations, station coverage intervals of very short duration, and even the complete absence of deflection data from certain antennas (necessitated by inoperative monitoring cameras in RAE-A). Before describing these capabilities, however, the immediate task is to apply the classical statistical approach to the dynamics specifically under consideration, and to illustrate feasibility of the over-all basic procedure.

Analysis

The mathematical background for most of the dynamic formulation is covered by the studies previously referenced. However, for an operational program, some extensions of the dynamic model are required: 1) the viscous damping in the Lagrangian analysis[2,3] must be replaced by a more realistic representation of the saturating magnetic hysteresis device; 2) if the four antenna booms have nonuniform thermal characteristics,** the pertinent portions of Ref. 3 need to be modified accordingly; and 3) some minor modifications of the analytical and computational procedure are needed. These topics are discussed prior to exposition of the theoretical background for the data processing scheme. Notation is consistent with Refs. 2 and 3.

** Due to the processes used, the effective thermal absorptivities are not measured easily. The booms are perforated and an absorptive coating is applied to the interior, in an effort to match the interior absorption to that of the exterior surface (which is highly reflective but has a greater area exposed to direct heat radiation).

Dynamic Model Extensions

To offset the increased complexity arising from nonuniform thermal characteristics, the operational dynamics program contains certain simplifications deemed permissible by analytical and numerical considerations. At RAE altitude (nearly one earth radius), the direct earth and reflected solar heat contribute only about 10% of the total heat flux; also, the terms contributed to $[\Delta k_t]$ by Eqs. (28) and (30) of Ref. 3 do not markedly influence RAE dynamics under operational conditions, and a similar case can be made for the entire matrix $[\Delta k_s]$. Therefore, while no implications upon general cruciform behavior are intended, all of the terms previously mentioned are omitted from the immediate formulation.

With the ith antenna absorptivity denoted as a_i, the corresponding thermally induced curvature then becomes simply $\mathfrak{K}_i = \beta_i \mathbf{p}_i' \times (\mathbf{p}_i' \times \boldsymbol{\delta})$, where

$$\beta_i \triangleq a_i e d J_s/(4\kappa Z) \tag{1}$$

so that Eq. (8) of Ref. 3 can be replaced by

$$\Psi_{tj} = EI \sum_{i=1}^{4} \int_0^l \frac{\partial}{\partial \chi_j} \left\{ -\beta_i \mathbf{p}_i'' \cdot \boldsymbol{\delta} + \frac{1}{2} \beta_i^2 (\mathbf{p}_i' \cdot \boldsymbol{\delta})^2 \right\} du \tag{2}$$

Following the procedure in Ref. 3 while retaining only the terms of interest, the resulting zero-order forces are

$$\Psi_{t0j} = EI\{\boldsymbol{\delta}_0^T [L_0] \boldsymbol{\delta}_{I,j} - \boldsymbol{\delta}_{I,j}^T \boldsymbol{\lambda}_0\}, \ 1 \leqslant j \leqslant 3 \tag{3}$$

$$\Psi_{t0j} = EI\{\boldsymbol{\delta}_0^T [L_{Ij}] \boldsymbol{\delta}_0 - \boldsymbol{\delta}_0^T \boldsymbol{\lambda}_{Ij}\}, \ 5 \leqslant j \leqslant 12 \tag{4}$$

and the desired augmenting matrix elements are

$$[\Delta k_t]_{jn} = [\Delta k_t]_{nj} = EI\{\boldsymbol{\delta}_{I,j}^T \boldsymbol{\lambda}_{In} - \boldsymbol{\delta}_0^T [L_{In}] \boldsymbol{\delta}_{I,j} - \boldsymbol{\delta}_{I,j}^T [L_{In}] \boldsymbol{\delta}_0\} \quad 1 \leqslant j \leqslant 3, \ 5 \leqslant n \leqslant 12 \tag{5}$$

with the modified definitions

$$\boldsymbol{\lambda}_0 = \sum_{i=1}^{4} \beta_i \mathbf{p}_{i0}' \Big|_{u=l} \qquad \boldsymbol{\lambda}_{Ij} = \sum_{i=1}^{4} \beta_i \mathbf{p}_{iI,j}' \Big|_{u=l} \tag{6}$$

$$[L_0] = \sum_{i=1}^{4} \beta_i^2 \int_0^l \mathbf{p}_{i0}' \mathbf{p}_{i0}'^T du, \ [L_{Ij}] = \sum_{i=1}^{4} \beta_i^2 \int_0^l \mathbf{p}_{i0}' \mathbf{p}_{iI,j}'^T du \tag{7}$$

The dynamics under consideration will then take the form

$$[m]\ddot{\chi} + [d]\dot{\chi} + [k + \Delta k_t]\chi = \boldsymbol{\Psi}_0 \tag{8}$$

where, as in Ref. 3, all coefficients and forcing function elements are held fixed for short-term intervals which can be cascaded. The matrix $[d]$ is now completely skew-symmetric (i.e., $d_{44} = 0$) and the magnetic hysteresis damping action is taken into account by including in $\boldsymbol{\Psi}_0$ a generalized force component $\boldsymbol{\Psi}_d$;

$$\boldsymbol{\Psi}_0 = \boldsymbol{\Psi}_e + \boldsymbol{\Psi}_{s0} + \boldsymbol{\Psi}_{t0} + \boldsymbol{\Psi}_d, \ \boldsymbol{\Psi}_d \triangleq \begin{bmatrix} \mathbf{0}_{3\times 1} \\ \pm T_m \\ \mathbf{0}_{8\times 1} \end{bmatrix} \tag{9}$$

where the scalar damping torque T_m is allowed to change polarity at appropriate boundaries of the fixed-parameter time intervals. Fortunately an RAE data tape provides repetitive measurements of the damper angle; straightforward location of smoothed extrema defines all of the damper torque polarity switching points needed in the dynamic model (the model then simulates a passive device, having negligible deadband, which generates a fixed magnitude torque always opposing the derivative of the smoothed damper angle waveform).

The fixed-parameter interval boundaries are conveniently selected as regular subintervals between each pair of consecutive damper switching events.

For greater accuracy in the computation it was found advantageous to scale the time (by the orbital mean motion) and the flexural state variables (normalized with respect to antenna length). Similar procedures were found beneficial in the parameter estimation and bias detection operations discussed subsequently. The necessary modifications are straightforward, however, and are excluded here for brevity.

Estimation of Satellite Dynamics

Application of Eqs. (8) and (9) to weighted-least-squares data processing can now be described as follows. The total time history of all data (including damper indicator, sun sensor, and magnetometer readings, plus the intermittent boom tip information) is divided into data blocks, of duration commensurate with the expected data fitting capability of the dynamical model as previously explained. The time at the start of a data block is denoted $t_{E(1)}$; the damper switching "events" determined from a central body data tape are then labeled consecutively $t_{E(2)}$, $t_{E(3)}$, . . . $t_{E(N_E-1)}$, where (N_E) represents the total number of events occurring within the block (the last event is taken as the end of the chosen data block). The time period between each event pair is then subdivided, according to a controllable maximum orbital mean anomaly increment, into linearized state transition intervals. The boundaries of these intervals are labeled in consecutive order as†† $\tau_1, \tau_2, \ldots \tau_{(N_T)}$; between any two boundaries the dynamic behavior is governed by Eqs. (8) and (9) which can be transformed into [see Eq. (59) of Ref. 2]

$$\mathbf{X} = [B_i]\mathbf{X} + \begin{bmatrix} 0_{12\times 1} \\ [m_i]^{-1}\mathbf{\Psi}_{0i} \end{bmatrix}, \quad \tau_{i-1} \leqslant t \leqslant \tau_i \tag{10}$$

where the matrix subscript signifies that $[m]$ and $[B]$, computed from the augmented matrices in (8), are valid for only the (ith) interval; similarly, $\mathbf{\Psi}_{0i}$ represents the right of Eq. (8) during the (ith) interval. The closed-form solution to (10) is

$$\mathbf{X}_m = [\Phi_{m,i-1}]\mathbf{X}(\tau_{i-1}) + \boldsymbol{\varphi}_{m,i-1}, \qquad \tau_{i-1} \leqslant t_m \leqslant \tau_i \tag{11}$$

where

$$[\Phi_{m,i-1}] \triangleq \exp\{[B_i](t_m - \tau_{i-1})\}, \quad \tau_{i-1} \leqslant t_m \leqslant \tau_i \tag{12}$$

(which is readily computed from the diagonalizing matrix and the eigenvalues of $[B_i]$), and

$$\boldsymbol{\varphi}_{m,i-1} \triangleq \{[\Phi_{m,i-1}] - [I]_{24\times 24}\}[B_i]^{-1}\begin{bmatrix} 0_{12\times 1} \\ [m_i]^{-1}\mathbf{\Psi}_{0i} \end{bmatrix} \tag{13}$$

The notation $\mathbf{X}_m$ conveniently is defined as the state at the time of the mth measurement (which in practice is the center of a prefiltering subinterval, during which several closely spaced observations are simply averaged) except for $m = 0$ $\{\mathbf{X}_0 \triangleq \mathbf{X}(\tau_0) = \mathbf{X}(t_{E(1)})\}$. Physically, Eq. (13) represents the change in state produced at (t_m) by the forcing function applied at (τ_{i-1}) and held fixed between (τ_{i-1}) and (t_m); it is easily verified that

$$\mathbf{X}_m = [\Phi_{m,0}]\mathbf{X}_0 + \boldsymbol{\varphi}_{m0}, \quad \tau_{i-1} \leqslant t_m \leqslant \tau_i \tag{14}$$

where, for $j = 0,1,2, \ldots$, the cascaded transition matrix is

$$[\Phi_{m,j}] = [\Phi_{m,i-1}] \prod_{k=j}^{i-2} [\Phi_{k+1,k}] \tag{15}$$

and the integrated force vector is

$$\boldsymbol{\varphi}_{m,j} = \sum_{n=j}^{i-2} [\Phi_{m,n+1}]\boldsymbol{\varphi}_{n+1,n} + \boldsymbol{\varphi}_{m,i-1} \tag{16}$$

†† $\tau_{(N_T)}$ represents the time at the end of this block, and τ_0 is set equal to $t_{E(1)}$; nonuniform intervals present no problem in the formulation.

The equations of motion are now in a form appropriate for computing the dynamic behavior from the measurements taken within any data block. For the complete set of (M) data vectors $(\hat{\mathbf{Y}}_m;\ m = 1,2, \ldots, M)$ in the block, having first-order sensitivities $[H_m] = \partial \mathbf{Y}_m^{(-)}/\partial \mathbf{X}_m$ and error covariance matrices $[Q_m]$, the notation $(\hat{\mathbf{y}}_m \triangleq \hat{\mathbf{Y}}_m - \mathbf{Y}_m^{(-)})$ will denote the mth residual vector (i.e., deviation from the predicted value $\mathbf{Y}_m^{(-)}$ which is computed from the a priori initial estimate $\mathbf{X}_0^{(-)}$, using Eq. (14) for extrapolation to time t_m). The weighted least-squares relation for the estimated initial state deviation $(\hat{\mathbf{x}}_0 \triangleq \hat{\mathbf{X}}_0 - \mathbf{X}_0^{(-)})$ would then be

$$\frac{\partial}{\partial \hat{\mathbf{X}}_0} \sum_{m=1}^{M} \{[H_m]\hat{\mathbf{x}}_m - \hat{\mathbf{y}}_m\}^T [Q_m]^{-1}\{[H_m]\hat{\mathbf{x}}_m - \hat{\mathbf{y}}_m\} = \mathbf{0}_{24\times 1} \tag{17}$$

under the condition that $\hat{\mathbf{X}}_m$ is related to $\hat{\mathbf{X}}_0$ by Eq. (14). The well-known quadratic form minimization estimate is

$$\hat{\mathbf{X}}_0 = \mathbf{X}_0^{(-)} + \left\{\sum_{m=1}^{M} [\mathfrak{M}_m]^T [Q_m]^{-1}[\mathfrak{M}_m]\right\}^{-1} \times \sum_{m=1}^{M} [\mathfrak{M}_m]^T [Q_m]^{-1}\hat{\mathbf{y}}_m \tag{18}$$

where $[\mathfrak{M}_m] \triangleq [H_m][\Phi_{m,0}]$. Instead of relying upon complete knowledge of the physical system, however, it is customary to extend the procedure to include uncertainties in parameter values and/or systematic measurement errors. Following is a description of the augmented state formulation, as applied to the present problem.

Parameter Estimation and Bias Detection

If the antenna absorptivities and the flexural rigidity (EI) are not known precisely, the dynamic model accuracy could suffer appreciably from inexact parameter values in (10). To counteract the resulting estimation error, the product $[\mathcal{G}]\tilde{\boldsymbol{\mathcal{E}}}$ is added to the right of (10), where $\tilde{\boldsymbol{\mathcal{E}}}$ is a 5×1 vector of uncertainties $(\tilde{\beta}_1, \tilde{\beta}_2, \tilde{\beta}_3, \tilde{\beta}_4, \tilde{EI})$ and $[\mathcal{G}]$ contains all forcing function partial derivatives with respect to $\boldsymbol{\mathcal{E}}$. Wherever these partial derivatives are functions of time or components of $\mathbf{X}$, they can be held constant during the interval denoted in (10); it follows that the resulting dynamics, written in the canonical form,

$$\frac{d}{dt}\begin{bmatrix} \mathbf{X} \\ \tilde{\boldsymbol{\mathcal{E}}} \end{bmatrix} = \begin{bmatrix} [B_i] & [\mathcal{G}_i] \\ [0]_{5\times 29} & \end{bmatrix}\begin{bmatrix} \mathbf{X} \\ \tilde{\boldsymbol{\mathcal{E}}} \end{bmatrix} + \begin{bmatrix} \mathbf{0}_{12\times 1} \\ [m_i]^{-1}\mathbf{\Psi}_{0i} \\ \mathbf{0}_{5\times 1} \end{bmatrix} \tag{19}$$

will also have a closed-form solution similar to an augmented version of (11). It is convenient to combine this with steady bias errors b_1, b_2, b_3 in the three magnetometers, so that the augmented state vector

$$\mathbf{X}^* \triangleq \begin{bmatrix} \mathbf{X} \\ \tilde{\boldsymbol{\mathcal{E}}} \\ \mathbf{b} \end{bmatrix} \tag{20}$$

will conform to the dynamic relation

$$\mathbf{X}_m^* = [\Phi_{m,i-1}^*]\mathbf{X}^*(\tau_{i-1}) + \boldsymbol{\varphi}_{m,i-1}^* \tag{21}$$

where

$$[\Phi_{m,i-1}^*] = \begin{bmatrix} [\Phi_{m,i-1}], & [G_{m,i-1}], & [0]_{24\times 3} \\ [0]_{5\times 24}, & [I]_{5\times 5}, & [0]_{5\times 3} \\ [0]_{3\times 24}, & [0]_{3\times 5}, & [I]_{3\times 3} \end{bmatrix} \tag{22}$$

$$[G_{m,i-1}] = \{[\Phi_{m,i-1}] - [I]_{24\times 24}\}[B_i]^{-1}[\mathcal{G}_i] \tag{23}$$

and

$$\boldsymbol{\varphi}_{m,i-1}^* = \begin{bmatrix} \boldsymbol{\varphi}_{m,i-1} \\ \mathbf{0}_{3\times 1} \end{bmatrix} \tag{24}$$

Just as $[\Phi]$ and $\boldsymbol{\varphi}$ can be referred to zero time by (15) and (16), respectively (and recursively computed in practice to

avoid growing memory calculations), a relation similar to (16) holds for the integrated parameter sensitivity matrix in (23). It is therefore a straightforward procedure to form the augmented transition matrix $[\Phi_{m,0}{}^*]$ referred to zero time, and combine it with the data vector sensitivity to the augmented state

$$[H_m{}^*] = \begin{bmatrix} [H_m], & [0]_{14\times 5}, & [I]_{3\times 3} \\ & & [0]_{11\times 3} \end{bmatrix} \tag{25}$$

so that, with $[\mathfrak{M}_m{}^*] \triangleq [H_m{}^*][\Phi_{m,0}{}^*]$ replacing $[\mathfrak{M}_m]$ in (18), all 32 unknowns can be determined by the canonical iterative weighted least-squares data processing.

It remains to show specifically how the matrix $[\mathcal{G}_i]$ is evaluated. From definitions of the various pertinent quantities it follows that, for $1 \leqslant k \leqslant 4$, the kth column is

$$[\mathcal{G}_i]_k = \frac{\partial}{\partial \beta_k}\left\{\begin{bmatrix} [0]_{12\times 12} & [I]_{12\times 12} \\ -[m_i]^{-1}[k_i + \Delta k_i], & -[m_i]^{-1}[d_i] \end{bmatrix}\begin{bmatrix} \chi \\ \dot{\chi} \end{bmatrix} + \begin{bmatrix} \mathbf{0}_{12\times 1} \\ [m_i]^{-1}\boldsymbol{\Psi}_{0i} \end{bmatrix}\right\}$$

$$1 \leqslant k \leqslant 4,\ \tau_{i-1} \leqslant t \leqslant \tau_i \tag{26}$$

This can be reduced by noting that 1) only the thermal portion of the generalized force contributes a nontrivial differentiable component to the last term, and 2) this zero-order component contains most of the thermal effect. Hence the simplification

$$[\mathcal{G}_i]_k \doteq \begin{bmatrix} \mathbf{0}_{12\times 1} \\ [m_i]^{-1}\partial\boldsymbol{\Psi}_{t0}/\partial\beta_k \end{bmatrix},\ 1 \leqslant k \leqslant 4,\ \tau_{i-1} \leqslant t \leqslant \tau_i \tag{27}$$

where $\boldsymbol{\Psi}_{t0}$ is computed from (3) and (4) with $\mathbf{o}_0$ and $\mathbf{o}_I$ evaluated at the center of the ith time interval. The derivatives with respect to β_k follow easily from (6) and (7).

At first glance it might seem that approximating (26) by (27) precludes a complete determination of the thermal parameter uncertainties. With the present computational approach, however, the entire dynamic model is adjusted after every weighted least-squares iteration; the partial correction omitted on one iteration can be uncovered during those following. So long as the computational weights are near the theoretical sensitivities, no difficulty with convergence or final accuracy will result.

The fifth column of $[\mathcal{G}_i]$ can be determined by writing the equations of motion with the true potential energy terms decomposed as

$$V_I = \hat{V}_I - \tilde{V}_I,\ V_{II} = \hat{V}_{II} - \tilde{V}_{II} \tag{28}$$

where the circumflex and tilde denote estimated values (i.e., the values obtained using the estimated flexural rigidity) and uncertainty (i.e., error in estimated values), respectively. For clarity the equations will be expressed for the case of no damper torque, solar pressure, or thermal effects (all of which can be added separately by superposition);

$$d/dt(\partial T_{II}/\partial\dot{\chi}) - \partial T_{II}/\partial\chi + \partial\hat{V}_{II}/\partial\chi = -\{d/dt(\partial T_I/\partial\dot{\chi}) + \partial(T_I - \hat{V}_I)/\partial\chi\} + \partial\tilde{V}_I/\partial\chi + \partial\tilde{V}_{II}/\partial\chi \tag{29}$$

The bracketed quantity on the right is recognized from the equilibrium formulation‡‡ of Ref. 2 and, again, the iterative computation permits various simplifying approximations. 1) The last term can be dropped, since it is overshadowed by the one preceding; thus

$$[\mathcal{G}_i]_5 \doteq -\begin{bmatrix} \mathbf{0}_{12\times 1} \\ [m_i]^{-1}\partial/\partial(EI)\{\partial V_I/\partial\chi\} \end{bmatrix} \tag{30}$$

and 2) in substituting Eq. (49) of Ref. 2 the derivative is approximated as $(2K_AK_{01}/EI)\mathbf{1}_8$. In practice these simplifications allow determination of flexural rigidity from the in-plane static deflections alone.

‡‡ More specifically, the bracketed quantity corresponds essentially to the static deflection computation[2] with the estimated value of flexural rigidity. The remaining terms on the right are effective forcing functions arising from imperfect knowledge of this parameter. Note that acceptability of approximating $[\mathcal{G}]$ in an iterative loop is again exploited, in the failure to decompose the kinetic energy similar to Eq. (28).

Simulation Approach

A model of RAE flexural, rotational, and hysteresis damper dynamics has been augmented by measurement relationships, to generate hypothetical data in the form of typical inputs for the operational estimation program. This form is dictated by the ground rules of the estimation program which called for inclusion of smoothed orbit tracking and damper data, with the latter controlling the choice of short-term dynamics time zone barriers. Operational compatibility calls for a somewhat modified astronomical description; Eq. (21) of Ref. 3 is changed to account for earth orbit eccentricity; the fraction of solar pressure and solar heat flux present (in the event of partial eclipse) is computed from finite disc size, and the transformation matrix in Eq. (22) of Ref. 3 is computed directly from Cartesian orbit position and velocity vectors. Errors due to direct extrapolation of smoothed navigation data and ephemeris data (e.g., perihelion time in 1968 or reference sidereal time used for magnetic field computation) are negligible in comparison with measurement uncertainties. Also, a Keplerian orbit model is adequate for this entire operation since 1) orbital perturbations will affect both the actual and the estimated dynamics in essentially the same fashion, and 2) available tracking data will allow patched conic fitting with frequent updating in practice. With these thoughts in mind, fictitious data for simulation purposes were generated by the procedure which follows.

Generation of Hypothetical Data

To simulate the orbital tracking data inputs, Cartesian position and velocity vectors are first determined at various epoch times (t_{REF}; not synchronized with other observational data) for a satellite in an orbit having 1) a semimajor axis of 12,380 km; 2) orbital inclination (i_0) and nodal longitude (Ω_0) chosen to provide (among other mission considerations) favorable solar exposure; 3) an initial satellite placement (as defined by a perigee time t_0 and argument ω_0) chosen for TV boom tip data coverage by the Rosman, N.C. station at a specified universal time (t_{ES}) on a given calendar day (t_{ED}), at the start of a data block. These conditions, combined with any initial state ($\mathbf{X}_0$, a 24 × 1 vector of initial generalized coordinates plus their time derivatives) and orbital eccentricity (e_0), determine a unique set of damper switching instants ($t_{E(j)}$) which are found from a separate dynamics program run trial. The interval between the (j)th and the $(j+1)$st damper switching event is subdivided into (I_j) time zones, where

$$I_j \triangleq \text{lowest integer} \geq \{[t_{E(j+1)} - t_{E(j)}]N_\theta/T_0\} \tag{31}$$

in which T_0 represents the orbital period and N_θ dictates the allowable length of fixed-parameter zones in the analytical model (e.g., for $N_\theta = 18$ the maximum mean anomaly increment between parameter updates would be $360°/18 = 20°$). There is a specified number (m_θ) of measurement prefiltering subintervals in each time zone and, at the center (t_m) of each subinterval, the following quantities are computed: 1) Cartesian position vector for the satellite at time (t_m), obtained by Keplerian extrapolation of position and velocity at an epoch time t_{REF} (in practice, t_{REF} is a time point slightly earlier than the most recent time zone barrier); 2) the current $\mathbf{X}_m$ (as determined using the *actual* flexural rigidity and

thermal absorptivities); 3) the sunline $\mathbf{\delta}_L$ expressed in local coordinates; 4) earth latitude λ_0 and longitude ψ_0 of the subsatellite point; 5) the magnetic field[9] vector $\boldsymbol{\beta}_L$ expressed in local coordinates; 6) a logic indicator which determines presence or absence of boom tip TV coverage (the condition for coverage being a satellite sightline within a 10°-above-horizon cone centered about an active station; any combination of seven TV stations can be activated in the simulation: Madagascar; Ororal, Australia; Alaska; Mojave, N.M.; Rosman, N.C.; Santiago, Chile; and Winkfield, England); 7) the direction cosine transformation $[C']$ between hub principal axes and local coordinates [see Eq. (4) of Ref. 2]; 8) random noise-corrupted values $\hat{Y}_i$ for components of the earth's magnetic field, as seen by instruments with sensitive axes along the unit vectors $\mathbf{A}_1$, $\mathbf{A}_2$, $\mathbf{A}_3$,

$$\hat{Y}_i = \mathbf{A}_i{}^T[C']^T\boldsymbol{\beta}_L + \tilde{Y}_i, \; 1 \leqslant i \leqslant 3 \tag{32}$$

where $\tilde{Y}_i$ is a Monte-Carlo Gaussian random number with a mean value equal to the simulated magnetometer bias and standard deviation (σ_F) corresponding to prefiltered magnetometer measurement accuracy; 9) a noise-corrupted damper angle measurement $\hat{Y}_4 = X_4 + \tilde{Y}_4$, where the random number $\tilde{Y}_4$ is generated from the Gaussian distribution of prefiltered damper indicator measurement errors (zero mean and standard deviation σ_D); 10) in-plane and out-of-plane antenna tip deformations computed from X_5–X_{12}, the 8×8 orthogonal transformation to W_1–W_8, and the static deflections K_A, K_B [again, an independent Gaussian variate is added to each, from a zero mean population with standard deviation σ_W; when the logic indicator described in item 6 dictates no current TV coverage, these "measured values" are replaced by unrealistically large numbers which will be eliminated through subsequent data rejection, see Eq. (34)]; 11) measured angles between a sun sensor face plane unit normal ($\mathbf{L}$) and the projection of the sunline $\{[C']^T\mathbf{\delta}_L = \mathbf{\delta}$ in vehicle coordinates$\}$ on a plane containing $\mathbf{L}$ and a sensor slit unit vector $\mathbf{U}_i$,

$$Y_{i+12} = \text{Arcsin}\left\{ \text{sgn}(\mathbf{\delta}\cdot\mathbf{U}_i)\left|\mathbf{L} \times \frac{(\mathbf{\delta}\cdot\mathbf{U}_i)\mathbf{U}_i + (\mathbf{\delta}\cdot\mathbf{L})\mathbf{L}}{|(\mathbf{\delta}\cdot\mathbf{U}_i)\mathbf{U}_i + (\mathbf{\delta}\cdot\mathbf{L})\mathbf{L}|}\right|\right\}_{i=1,2} \tag{33}$$

$$\hat{Y}_{i+12} = Y_{i+12} + \tilde{Y}_{i+12}$$

in which the probability distribution of $\tilde{Y}_{i+12}$ is Gaussian with zero mean and standard deviation σ_S for prefiltered sun sensor measurement errors.

The output generated by this program consists of an initial record (defining the total number M of data vectors; the number m_θ of data vectors per time zone; the values t_{ED} and t_{ES} which mark the start of the data block; plus the time at the end of the data block and all damper switching times there within) and the complete set of M data records. Each data record contains 1) the measurement time t_m, 2) the most recent time zone barrier τ, 3) the polarity of the damper angle derivative, 4) the currently used orbit tracking epoch time t_{REF}, 5) Cartesian position and velocity vectors of the composite satellite mass center at t_{REF}, 6) the fourteen-dimensional data vector $\hat{\mathbf{Y}}$, and 7) an index number identifying which of the eight RAE sun sensors measured the last two components of $\hat{\mathbf{Y}}$. The information is arranged in the same format designed for an actual RAE "composite data" file, prepared for the operational estimation program described below.

Postdeployment Operational Program

A weighted-least-squares (WLS) estimate is computed for the augmented state at data block initiation, on the basis of the measurements within the block, the functional relations between these measurements and the state, the covariance matrix of prefiltered measurement errors, and the dynamical and astronomical models employed. A time history is generated from this initial state estimate and, depending upon the residuals obtained, the measurement data may be recycled up to a controllable maximum number (N_I) of iterations. A favorable a priori estimate for $\mathbf{X}_0$ will theoretically reduce the residuals for any given iteration number but, due to the existence of a preferred reference state, the a priori estimate input can be incomplete as previously explained.

After introduction of the various fixed quantities (astrodynamical constants, sensor parameters, etc.) and initialization (for accumulated residuals, state transition identity matrix, etc.), the estimation program performs the following steps:

1) One data record is read from the composite data file.

2) For the period between the first two entries (t_m, τ) of this record, all state transition elements (of $[\Phi]$, $[G]$ and φ) are determined by a subroutine containing the complete closed form dynamics computation (using estimated values for flexural rigidity and thermal absorptivities). The transition back across all time zones to the data block initialization time is then obtained by recursion.

3) The current estimated state $\hat{\mathbf{X}}_m$ is computed from (14) using the value of $\hat{\mathbf{X}}_0$ from (18) on the last WLS iteration (or from the a priori estimate during the first iteration).

4) The satellite position at (t_m) is calculated by Keplerian extrapolation of the position and velocity at the epoch time (t_{REF}) on the current data record.

5) The sunline at (t_m) is computed and expressed in local coordinates.

6) The subsatellite point is located on the earth and the local magnetic field $\boldsymbol{\beta}_L$ is computed with the aid of a NASA-Goddard subroutine.[9]

7) The direction cosine matrix $[C']$ and its partial derivatives $\partial[C']/\partial X_j$ are evaluated at (t_m).

8) From the current estimated state $\hat{\mathbf{X}}_m$ the 14 components of the predicted data vector $\mathbf{Y}_m{}^{(-)}$ are evaluated. A maximum absolute value Y_L is specified for observable fractional field components $Y_i/|\boldsymbol{\beta}_L|$, $1 \leqslant i \leqslant 3$; for the damper angle Y_4; and for the relative tip deformations W_i/l, $1 \leqslant i \leqslant 8$; a minimum value of $(\pi/2 - Y_L)$ is specified for the angle defining the slit-sunline planes defined in Eq. (33). Any measurement with a predicted value outside the specified range is rejected on grounds of poor conditioning.[8] For each accepted measurement the residual is computed and tested vs a "3-sigma limit" (R_L) prescribed as follows. Since the division between acceptable and unacceptable residual size is not defined precisely, a suitable criterion can be obtained from the rms level which would result from an instrument error combined with independent estimation error components (using the same value σ_u for rms uncertainty in all estimated angles $\hat{X}_1$–$\hat{X}_4$ and in relative tip deflections $\hat{X}_5/l$–$\hat{X}_{12}/l$; in this program a larger value σ_{u1} is used for the first WLS iteration, followed by substitution of a tighter limit σ_{u2} afterward). Thus the computation for R_L becomes

$$R_{L(i)} = 3[(\sigma_u l)^2 + \sigma_W{}^2]^{1/2}, \; 5 \leqslant i \leqslant 12 \tag{34}$$

or

$$R_{L(i)} = 3\left[\sigma_u{}^2 \sum_{j=1}^{12} H_{ij}{}^2 + \sigma_i{}^2\right]^{1/2}, \; 1 \leqslant i \leqslant 4 \text{ or } i = 13, 14 \tag{35}$$

where σ_i takes the value

$$\sigma_i = \sigma_F, \; 1 \leqslant i \leqslant 3, \; \sigma_4 = \sigma_D, \; \sigma_{13} = \sigma_{14} = \sigma_S \tag{36}$$

and the previously defined sensitivities H_{ij} are evaluated from the functional relations described in items 8–11 of the preceding section {e.g., $H_{ij} = \mathbf{A}_i{}^T(\partial[C']^T/\partial X_j)\boldsymbol{\beta}_L$, $1 \leqslant i, j \leqslant 3$; $H_{44} = 1$; sun sensor derivatives are illustrated for a different sensor mechanization and Euler angle conveniont in Ref. 8}.

The cumulative matrix and vector computation implied in Eqs. (18, 22, and 25) is carried out for each properly conditioned data vector component having an acceptable residual; also summed over ($1 \leqslant m \leqslant M$) are the number $N_{p(i)}$ of these accepted observations for each measuring device ($1 \leqslant i \leqslant 14$), and the values of the normalized residuals (y_{mi}/σ_i) and their squares. This latter summation

$$R^2 = \sum_{i=1}^{14} \sum_{m} \left(\frac{\hat{y}_{mi}}{\sigma_i} \right)^2 \tag{37}$$

(with the rejected data points excluded) is then tested vs a chi-squared distribution having

$$N_f = \left[\sum_{i=1}^{14} N_{p(i)} \right] - 32 \tag{38}$$

degrees of freedom[10]; for large N_f this is nearly Gaussian with mean and variance of N_f and $2N_f$, respectively. Separate algebraic sums of the residuals, not squared and not summed over (i), can be used in bias detection. Although the residuals are not all independent, the sum (again excluding rejected data)

$$R_i = \left[\sum_{m} \frac{\hat{y}_{mi}}{\sigma_i} \right] \Big/ N_{p(i)}^{1/2} \tag{39}$$

approaches the zero mean unity variance Gaussian distribution for large $N_{p(i)}$. This, however, is intended only as verification for absence of unduly large biases, and is to be distinguished from the classical systematic error rejection by the augmented state procedure mentioned earlier.

Numerical Results

Performance of the estimation program can be determined by three approaches: 1) verification through actual satellite data processing, 2) simulation of the data processor fed by hypothetical measurements,§§ and 3) linearized uncertainty covariance matrix analysis. Successful application of the first approach (as evidenced by residuals) would verify the model; the second approach (as evidenced by convergence of the estimate toward the dynamic path from which the simulated data were generated) verifies the linearization and establishes observability; the third approach predicts behavior of the statistical ensemble. Although a thorough validation requires all three of these operations, only the last two are included here. Unfortunately, the first is unavailable, because after full-length RAE antenna deployment, very few tip readings were obtained from one upper TV camera, and the lower boom tips could not be distinguished from the earth below. Thus, although the TV images provided both confirmation of stable attitude behavior (which had been verified in all three axes by sun sensor and magnetometer readings) and reasonable bounds for elastic antenna deformations, they did not permit a time history reconstruction at any time. (A one-orbit-duration antenna motion history requires at least one glance at the tips near the beginning, and another near the end, of the orbit.) Results from the two computational approaches now will be summarized.

Data Simulation

A simulation trial was made with the satellite starting from perigee at 12 hr UT on the 197th calendar day in an orbit having 0.02 eccentricity and an inclination, nodal longitude and perigee argument of 122°, 90°, and 45°, respectively. Under these conditions, with Rosman as the only active ground station, antenna tip data coverage is provided for approximately the first and the last 35 min of the 3.8 hr data block (one orbit). A 20° limit was chosen for the maximum mean anomaly increment between successive parameter updates, and each fixed-parameter zone was divided into five measurement prefiltering subintervals. Instrument error standard deviations, with prefiltering taken into account, were set at 0.06 rad, 0.015 rad, 0.01 rad, and 2 m for the magnetometers at the magnetic poles, the damper angle indicator, the sun sensors, and the antenna tip measurements, respectively. The data limit parameters σ_{u1}, σ_{u2}, and Y_L were set at 0.2, 0.05, and 0.5 rad, respectively. Satellite hub parameters, and the antenna length and wall thickness, were equal to the values corresponding to case 2 of Ref. 2; other parameter values chosen were: normalized hinge spring constant (~1.3), skew angle (66.5°), mass (4.22 kg), length (192 m), and moment of inertia (13,000 kg-m²) of the damper; antenna cantilever angle (27.9°), linear mass density 0.0208 kg/m), diameter (0.0145 m), and flexural rigidity (EI = 5.17 N-m²); and the viscous damping ratio was of course set to zero for replacement by the switched damping torque of 0.0142 N-m. Parameters affecting response to solar pressure and uneven heating were set at the values in Ref. 3 except for solar heat absorptivities of 0.10, 0.08, 0.06, and 0.04 in the four quadrants, respectively. To test the augmented state estimation capability the iterations were started with an estimated flexural rigidity of 6.6 N-m² and uniform estimated thermal absorptivities of 0.05; furthermore the x- and y-axis magnetometer readings were biased by unknown systematic errors equivalent to 0.05 and 0.08 rad, respectively, at the magnetic pole. The initial 12 × 1 vector of generalized coordinates[2] consisted of the following components, listed in order: 0.1, 0.1, 0.2, and 0.1 rad; and 2, 2, 5, 20, −15, 10, 10, and −5 m; all derivatives were zero except for an initial damper angle rate of -3×10^{-4} rad/sec. The iterative estimation program, however, was begun at an initial state set to zero throughout with the exception of an imperfect estimate of initial damper action (0.05-rad displacement and a rate of -2×10^{-4} rad/sec). It was felt that, if the system could "find itself" under these conditions, this would meet the basic requirements of the data processor.

The success of the estimation program can be judged from Figs. 1 and 2 which illustrate, respectively, the accuracy of attitude and damper time history estimation (from essentially continuous data), and reconstruction of elastic behavior (with highly intermittent boom tip data), after six weighted least-squares iterations. Actual and estimated state variables are represented by solid curves and crosses, respectively. Due to the previously described measurement subdivision within damper switching events, the abscissa does not quite correspond to a uniform time scale; it should be pointed out, however, that the main reason for nonsinusoidal flexural mode appearance is the thermal absorptivity mismatch. At any rate, the estimation program converged upon the actual state (even the smaller amplitude remaining flexural modes, not shown, were detected with comparable accuracy); also, the unknown parameters were determined to within 10% of their actual values, and the magnetometer biases were detected to accuracies well within the rms sensor errors.

Ensemble Performance

The simulation just described contains only one Monte Carlo sample, i.e., some variation in the results would be produced by merely shifting the random measurement error sequence. Obviously a more efficient approach is needed to characterize performance of a statistical population, especially when effects of parameter changes are to be studied. To fill this need, Eq. (18) of course automatically implies that

§§ This practice serves a greater purpose than mere program checkout. It establishes observability of the complete augmented state, provides an indication of estimation accuracy to be anticipated operationally, and validates the linearization (measurement sensitivity and dynamic partial derivatives are computed from the noise-corrupted estimated state).

Table 1 Rms antenna tip estimation errors

Case	Conditions	Rms uncertainty at peak, m			
		In-plane		Transverse	
		Upper	Lower	Upper	Lower
1	Standard ($N_C = 4$; $N_V = 2$; $N_S = 1$)	4.4	4.5	1.2	1.3
2	$\sigma_W = 0.5$	2.5	2.5	0.7	0.8
3	$N_S = 4$	0.9	0.9	0.6	0.6
4	$N_S = 4$, and $\sigma_A = 0.02$, $\sigma_D = 0.03$, $m_\theta = 20$	3.1	3.4	0.9	1.0
5	$N_V = 5$	0.7	0.7	0.6	0.6
6	$N_V = 5$, and $N_C = 2$	0.9	5.5	1.0	1.0
7	$N_C = 2$	5.9	9.4	1.9	2.1
8	$N_C = 2$, and $X_{01} = X_{02} = 0.1$, $X_{03} = 0.2$	5.6	6.6	1.6	1.9
9	Same as 8, but $a_1 = a_2 = a_3 = a_4 = 0.05$	5.9	7.2	1.8	2.2
10	Same as 8, but $a_1 = a_2 = a_3 = a_4 = 0$	7.1	8.7	2.4	2.4
11	Same as 8, but $\sigma_A = 0.001$	2.0	1.7	0.9	0.9
12	Same as 8, but $\sigma_D = 0.001$	3.9	4.6	1.3	1.3
13	$\sigma_W = 100$, $X_{01} = X_{02} = 0.1$, $X_{03} = 0.2$, and $\sigma_A = \sigma_D = 0.001$	1.9	1.8	4.2	4.2

the initial estimation uncertainty covariance matrix is¶¶

$$\langle \tilde{\mathbf{X}}_0 \tilde{\mathbf{X}}_0^T \rangle = \left\{ \sum_{m=1}^{M} [\mathfrak{M}_m]^T [Q_m]^{-1} [\mathfrak{M}_m] \right\}^{-1} \quad (40)$$

and, using linearized dynamics, the covariance matrix at any other time (t_m) is

$$\langle \tilde{\mathbf{X}}_m \tilde{\mathbf{X}}_m^T \rangle = [\Phi_{m,0}] \langle \tilde{\mathbf{X}}_0 \tilde{\mathbf{X}}_0^T \rangle [\Phi_{m,0}]^T \quad (41)$$

These last two expressions are determined completely by specification of dynamics, measurement accuracies, and sensitivities (via $[\Phi]$, $[Q]$, and $[H]$, respectively). Standard computational conditions for each are as follows.

1) All astronomical, orbital, and satellite parameters correspond to the previously described simulation case, except for zero eccentricity, zero hysteresis damper torque, zero initial state, unaugmented hub inertias, and 6.6 N-m² flexural rigidity.

2) The libration angles were assumed to be observed directly with rms errors $\sigma_A = 0.01$ rad. Errors in direct damper angle measurements and antenna tip observations were set at 0.015 rad and 1 m rms, respectively.

3) For all 90 data vectors (product of $N_\theta = 18 \times m_\theta = 5$, in the standard case), the first four components have sensitivities ($h_{ij} = \delta_{ij}$; $1 \leqslant i \leqslant 4$, $1 \leqslant j \leqslant 24$), where δ_{ij} is the Kronecker delta. Antenna measurement sensitivities are easily computed from the 8×8 orthogonal relationship (Table 1, Ref. 2), but these elements must be blanked whereever no TV camera coverage exists. In the present series of covariance matrix computation runs, antenna tip data coverage is defined in terms of the number N_C of operative cameras, the number N_V of ground station sightings, equally spaced in time, and the number N_S of consecutive tip measurements per sighting taken by each operative camera. Standard computation run conditions are $N_C = 4$, $N_V = 2$ (one sighting at the beginning and one at the end of the orbit), and $N_S = 1$.

Table 1 shows the levels of performance to be expected under various conditions. Unless otherwise specified, parameter values for each case conform to the standard just described (case 1). Covariances of individual boom tip uncertainties were obtained by transforming the appropriate partition from Eqs. (40) and (41) through the 8×8 orthogonal relation (Table 1, Ref. 2). Actually the estimation error varies along the orbit (with error peaks occurring at different points, depending upon conditions), and there is often as much difference (e.g., 40%) between the position uncertainties in the upper booms themselves as there is from upper to

¶¶ This corresponds to the unaugmented case; to characterize the basic data processor accuracy under various conditions (particularly limited antenna coverage) it is reasonable to focus upon operations occurring after the parameter variations have been determined. To circumvent inaccurate numerical inversions which could occur with low data coverage, Eq. (18) has been replaced by a generalized inverse formulation.[11] Although this important step significantly influenced the estimation program configuration, it is not discussed further here because 1) generalized inversions are widely accepted, and 2) they do not alter basic system capability, but only help to resist numerical degradation.

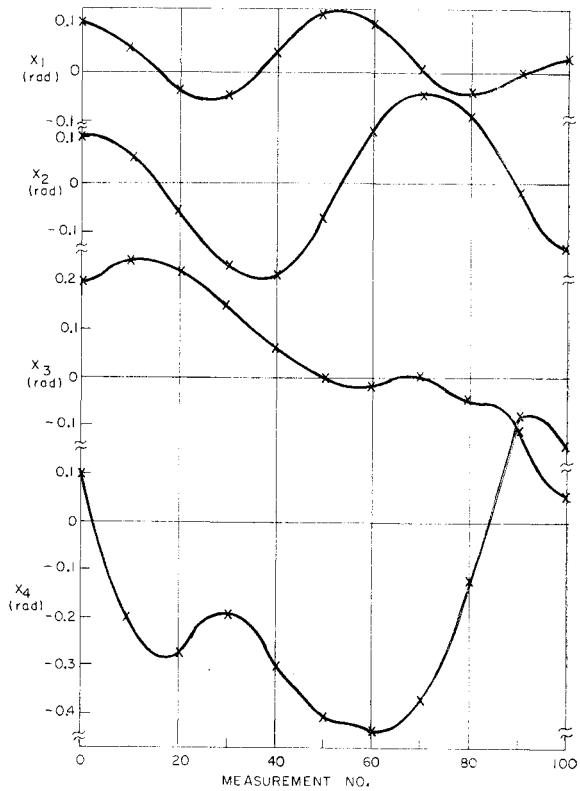

Fig. 1 Angular orientation vs time.

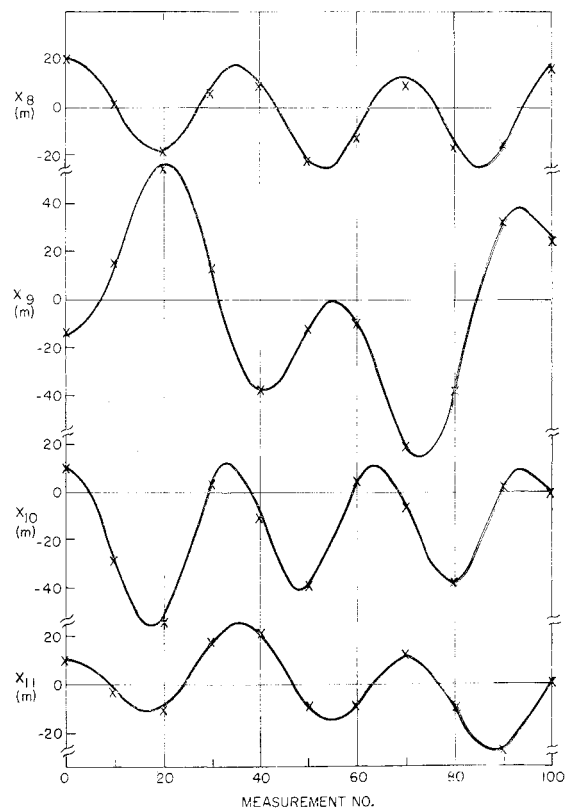

Fig. 2 Satellite deformation vs time.

lower; however a concise presentation of results, showing only the maximum upper and lower antenna tip position rms uncertainties, is adequate for expository purposes. Also, these maxima are just close approximations to the true peak uncertainties, since Eq. (41) and its subsequent computing operations are performed at discrete times (up to 20 times per orbit).

Comparison of cases 1 and 2 shows that, with the standard measurement schedule, antenna position uncertainty is only roughly proportional to σ_W; the departure from direct proportionality can be attributed to the coupled dynamic variables X_1–X_4 the rms accuracies of which were not changed between these two trials. It might have been expected that case 3 would yield results comparable to case 2, because an increase in the number of closely spaced statistically independent observations (by any factor R) is comparable to a reduction in rms measurement error (by a factor of $R^{1/2}$). The consecutive antenna data points in case 3, however, span an interval of about 8 min; thus they provide error reduction by reason of their spread. Case 4 is more nearly comparable to case 2. (Note that this corresponds to ~2-m in spans of antenna data, with equivalent angular measurement accuracy. To test this interpretation further, m_θ was again quadrupled with another twofold increase in σ_A and σ_D; results were in agreement with case 4.) Case 5 shows little improvement over case 3 when antenna observations are added at orbital mean anomaly positions of 90°, 180°, and 270°. This can be interpreted as verification that, with the known dynamic model, observability was already adequate under conditions of case 3. As illustrated by the next two cases, however, these additional antenna sightings would be quite useful when only the upper cameras are operative. (Proximity of upper and lower uncertainties in case 7–10 is due to dynamic coupling; without this there would be a small upper antenna position uncertainty, and a larger uncertainty for the lower antennas. Difference between in-plane and transverse error magnitudes will be discussed shortly.) Comparison of cases 7 and 8 illustrates a beneficial result introduced by increased dynamic coupling. Conversely, the next two cases demonstrate a reduction in observability which occurs when the unseen antennas are less tightly coupled to attitude. In varying degrees the last three cases verify the theoretical capability of accurate angular data to replace antenna observations; these are somewhat academic, since any attempt to accomplish this in practice would be quite sensitive to small imperfections in the dynamic model.

Comparison of in-plane and transverse uncertainty is worthy of further comment. For conditions producing antenna tip uncertainties far exceeding σ_W, estimation error can be explained in terms of ambiguities which arise when only two tips are visible (this excludes the last case, in which all antenna information is essentially suppressed). For example, a vertical mode of satellite deformation cannot be distinguished from the in-plane neutral mode, on the basis of upper camera sightings alone. Furthermore these modes are not too tightly coupled to attitude (as evidenced by the appropriate off-diagonal terms in the eigenvector matrix), and their natural frequencies (more specifically, the eigenvalues which correspond to their largest eigenvector components, the distinction being prompted by coupling between the generalized coordinates) are both in the same range as the oscillation rate most closely associated with still another loosely coupled in-plane mode, i.e., longitudinal. Inspection of the covariance matrices (not shown) directly computed from Eqs. (40) and (41), ahead of the 8×8 orthogonal similarity transformation used to generate Table 1, has verified that the major contributors to the in-plane antenna position uncertainty are the in-plane neutral, longitudinal, and vertical deformation modes, when only the upper cameras are operative. The other in-plane mode of satellite deformation (pitch) is more observable because all of its major spectral components are either 1) more tightly coupled to attitude, or 2) energy-limited at higher frequencies.

Because the energy-limiting/coupling phenomenon benefits only one in-plane mode, the 2-camera ambiguity remains unresolved. For transverse flexure, this benefit is enjoyed by two modes (roll and yaw). This helps to distinguish roll from lateral and yaw from transverse neutral when only the upper cameras are operative, and accounts for the smaller transverse uncertainties observed in general.

Before this discussion is terminated it is of interest to consider case 1 under conditions of Shannon waveform reconstruction[12] with no dynamic model. In order to account for all antenna oscillations up to 3.5 cycles/orbit (this would include the in-plane neutral and all translational flexural modes), the Shannon sampling rate would be 7 observations per orbit for each camera; however, this Shannon rate applies to infinite total duration, hardly the case for a single orbit. To achieve the rms accuracies of case 1 with $\sigma_W = 1$ m, it is quite likely that at least twenty (and quite possibly 30 or more) measurements per camera would be required during the orbit. Also, estimation of lower antenna positions in the last seven cases would obviously be impossible without the dynamic model. Thus the model reduces data rate requirements by an order of magnitude, and simultaneously enables estimation of unseen motion through dynamic coupling.

Conclusion

An iterative weighted least-squares estimation program has been developed and successfully tested, whereby the time history of coupled rotation and flexural behavior can be reconstructed from RAE data tapes. The program is capable of simultaneously detecting magnetometer bias errors and improving the determination of system parameters. Linearized ensemble statistics have evaluated estimation accuracy under various conditions of measurement availability.

References

[1] Stone, R. G., "RAE-1500 Foot Antenna Satellite," *Astronautics and Aeronautics*, Vol. 3, No. 3, March 1965, pp. 46–49.

[2] Newton, J. K. and Farrell, J. L., "Natural Frequencies of a Flexible Gravity Gradient Satellite," *Journal of Spacecraft and Rockets*, Vol. 5, No. 5, May 1968, pp. 560–569.

[3] Farrell, J. L. and Newton, J. K., "Solar Pressure and Thermal Effects on the Radio Astronomy Explorer," Paper 68-126, Sept. 1968, American Astronautical Society.

[4] Farrell, J. L., Newton, J. K., and Hedland, D. A., "Dynamics of Libration-Damped Discretized Cruciform Structure," *AIAA Structural Dynamics and Aeroelasticity Specialist Conference*, AIAA, New York, 1969, pp. 75–83.

[5] Farrell, J. L., Newton, J. K., and Connelly, J. J., "Digital Program for Dynamics of Non-Rigid Gravity Satellites," CR-1119, Aug. 1968, NASA.

[6] Hooker, W. and Margulies, G., "The Dynamical Equations for an n-Body Satellite," *Journal of the Astronautical Sciences*, Vol. XII, No. 4, 1965, pp. 123–128.

[7] Roberson, R. E. and Wittenburg, J., "A Dynamical Formalism for an Arbitrary Number of Interconnected Rigid Bodies, with Reference to the Problem of Satellite Attitude Control," Paper 46.D, London, June 1966, International Federation on Automatic Control.

[8] Farrell, J. L., "Attitude Determination by Kalman Filtering," *Proceedings of the IFAC Symposium on Automatic Control in Space*, Vienna, Austria, Sept. 1967, to be published; also CR-598, Sept. 1966, NASA.

[9] "Computer Programs for the Computation of B and L (May 1966)," National Space Science Data Center Users Note NSSDC-67-27, May 1967.

[10] Mood, A. M. and Graybill, F. A., *Introduction to the Theory of Statistics*, 2nd ed., McGraw-Hill, New York, 1963, pp. 348.

[11] Rust, B. et al., "A Simple Algorithm for Computing the Generalized Inverse of a Matrix," *Communications of the ACM*, Vol. 9, No. 5, May 1966, pp. 381–387.

[12] Oliver, B. M., Pierce, J. R., and Shannon, C. E., "Philosophy of PCM," *Proceedings of the Institute of Radio Engineers*, Vol. 36, No. 11, Nov. 1948, pp. 1324–1331.